Advanced Sustainable Systems

ADVANCED SUSTAINABLE SYSTEMS
www.advsustainsys.com

RESEARCH ARTICLE

Flaxseed-Based Green Electrolyte Enabling High Electrochemical Stability for Advanced Zinc Ion Batteries

Yigit Berke Arikan[1] | Gokce Komurcuoglu[1] | Sadaf Adhami[2] | Gulsah Yaman Uzunoglu[3,4] | Recep Yuksel[2,4,5]

[1]Department of Chemical Engineering, Eskisehir Osmangazi University (ESOGU), Eskisehir, Türkiye | [2]Department of Chemistry, Eskisehir Osmangazi University (ESOGU), Eskisehir, Türkiye | [3]Department of Chemical Engineering, Istanbul Health and Technology University (ISTUN), Istanbul, Türkiye | [4]Advanced Materials Technologies Application and Research Center (IMATEK), Eskisehir Osmangazi University (ESOGU), Eskisehir, Türkiye | [5]Nanoscience and Nanotechnology, Graduate School of Natural and Applied Sciences, Eskisehir Osmangazi University (ESOGU), Eskisehir, Türkiye

Correspondence: Gulsah Yaman Uzunoglu (gulsah.uzunoglu@istun.edu.tr) | Recep Yuksel (recep.yuksel@ogu.edu.tr)

Received: 26 November 2025 | **Revised:** 7 January 2026 | **Accepted:** 12 January 2026

Keywords: biomass-based electrolyte | dendrite suppression | flaxseeds | interfacial stability | Zn-ion batteries

ABSTRACT

This study presents a green and sustainable electrolyte derived from flaxseeds (FS) aimed at enhancing the electrochemical stability of zinc-ion batteries (ZIBs), thereby reducing the occurrence of free water molecules and alleviating the hydrogen evolution reaction (HER) that contributes to the development of zinc (Zn) dendrites. The abundant hydroxyl groups present in polysaccharides and phenolic compounds within the flaxseeds coordinate with Zn^{2+}, modifying the solvation sheath and reducing HER activity. Zn//Zn symmetric cells utilizing the FS-based electrolyte exhibited remarkably stable cycling for 3000 h at a current density of 1.0 mA cm^{-2} (1.0 mAh cm^{-2}) and 2500 h at 2.0 mA cm^{-2} (2.0 mAh cm^{-2}). Zn//V_2O_5 full cells delivered a discharge capacity of 233.8 mAh g^{-1} at 0.2 A g^{-1} and excellent rate capability across a wide current density range of 0.2–10 A g^{-1}. The ex situ SEM and XRD results confirmed uniform Zn deposition along the (002) plane without dendrite formation. This work demonstrates a biomass-derived, low-cost electrolyte formulation strategy that effectively stabilizes Zn interfaces, providing a green and efficient pathway for next-generation zinc-ion batteries.

1 | Introduction

Rechargeable zinc-ion batteries (ZIBs) have emerged as a promising option for future large-scale energy storage applications, experiencing substantial growth over the past decade. This growth can be attributed to their high capacity, the reversibility of the zinc (Zn) metal anode, cost-effectiveness, enhanced safety, and environmental sustainability [1]. Nonetheless, during the charge–discharge cycles of ZIBs employing traditional aqueous electrolytes, Zn is susceptible to uneven ion flux, resulting in the formation of Zn dendrites and byproducts linked to the hydrogen evolution reaction (HER). The parasitic side reactions, HER activity, corrosion, and anode passivation, within aqueous ZIBs undermine their cycling stability and overall cell performance [2]. Such limitations necessitate the formulation of alternative electrolyte systems capable of enhancing the stability and performance of ZIBs through precise modulation of ionic flux, ionic conductivity, electric-field homogeneity, and ion-solvation structure, while simultaneously emphasizing sustainability and environmental compatibility [3–5].

It is well established that the solvation structure of the electrolyte significantly influences the interfacial chemistry between the electrode and the electrolyte. In typical aqueous electrolytes for ZIBs, Zn^{2+} ions are generally solvated by water molecules in a strongly solvating manner, resulting in the formation of $[Zn(H_2O)_6]^{2+}$, while anions and the remaining unsolvated H_2O molecules are excluded from the solvation sheath. The presence

of this $[Zn(H_2O)_6]^{2+}$ species leads to a considerable energy barrier for the desolvation of Zn^{2+} ions, which may result in side reactions associated with water. Moreover, H_2 gas evolution alters the local pH and triggers the formation of passivation layers, such as $Zn(OH)_2$ and ZnO, which hinder ion and electron diffusion, reduce Zn utilization, and promote the growth of Zn dendrites [6]. The suppression of active water molecules enables the regulation of Zn^{2+} solvation and desolvation processes, thereby impacting the electrochemical performance of the Zn anode [7]. Therefore, it is crucial to suppress the side reactions in aqueous electrolytes to facilitate good reversibility of the Zn anode [8]. Particularly, compounds rich in hydroxyl groups interfere with the solvated configuration of $[Zn(H_2O)_6]^{2+}$ by utilizing a strategy of hydrogen bond competition, which penetrates the primary solvation shell of Zn^{2+} and substitutes water molecules [9].

In order to ensure the stability of Zn anodes, earlier research indicates that a hydrophilic Zn/electrolyte interface promotes uniform charge distribution and improves reaction kinetics, whereas a hydrophobic interface inhibits water-induced HER activity and Zn corrosion [10]. Biomass materials are defined by the presence of hydrophilic functional groups, including amine (NH_2), hydroxyl (—OH), ether (—COC), amide (—CONH or —$CONH_2$), which exhibit a strong affinity for polar molecules. In the context of biomass-derived electrolytes, these abundant active sites in biomass enable the electrolytes to modify the solvated structure, the electrical double layer, and the hydrogen bonding network, while mitigating the adverse effects of anions or water molecules. The presence of lone pair electrons on the oxygen and nitrogen atoms within these polar functional groups leads to significant interactions with water, thereby decreasing water activity. Moreover, these functional groups can serve as sites for hydrogen-bond networks, facilitating the formation of hydrogels from biomass materials that possess remarkable flexibility [4, 11].

Natural materials and their derivatives, obtained from renewable and sustainable resources, offer promising solutions to alleviate both HER activity and dendrite formation [12]. The structural diversity, enhanced surface chemistry, and considerable eco-friendliness of biomass materials position them as a promising alternative for the development of high-performance ZIBs (United Nations Sustainable Development Goals 7, 12 & 13) [13]. Natural organic compounds, including taurine, γ-valeolactone, [14] saccharides [15, 16], alkylpolyglycosides (APGs) [17], propylene glycol [18], trehalose [19] and organic acids including pytic acid [20] and tannic acid [21, 22] have recently been demonstrated to influence the solvation structure of the electrolyte and to improve the electrode/electrolyte interface of ZIBs [12]. As the first example of using biomass extraction in electrolyte formulation for ZIBs, Yuksel et al. developed an aloe vera-based green electrolyte with a quinone-rich composition, which significantly extended the electrochemical stability of the symmetrical Zn cell to 4500 h and enabled higher specific capacities at different current densities [23].

Flaxseed (FS, Linum usitatissimum L.), also known as linseed, is recognized as a functional food ingredient due to its numerous health benefits [24]. Flaxseed hydrogel has attracted considerable attention due to its exceptionally rich organic moiety and amphiphilic nature [24, 25]. The extraction temperature, the characteristics of the solvent, and the properties of the raw material influence the yield of hydrogel from flaxseeds [26]. Flaxseed hydrogel extracted with water at room temperature consists of phenolic acids, such as d-galacturonic, p-coumaric, caffeic, ferulic, chlorogenic, caffeic acid [24], quercetin, and disaccharides [27, 28], including *l*-galactose, galactose, *l*-rhamnose, and d-xylose [29]. The phenolic acids (e.g., ferulic, gallic, and coumaric acids) and sugar derivatives (such as rhamnose and galactose units) in flaxseed gel matrix contain abundant hydroxyl, ether, and carboxylate functionalities [30], which play a key role in coordinating Zn^{2+} ions, mitigating HER, and suppressing dendrite growth [31, 32], Hence, integrating FS-gel abundant in saccharides and phenolic molecules with zincophilic functional groups into the electrolyte formulation presents an effective route to modulate Zn^{2+} solvation, minimize parasitic reactions, and strengthen interfacial stability.

In this work, we developed a flaxseed (FS) gel-based electrolyte as a sustainable and efficient strategy to stabilize the anode/electrolyte interface in ZIBs. Unlike most previously reported biomass-based electrolytes, which rely on the precise blending of synthetic or isolated biomass-derived additives and solvents, the FS-based electrolyte system directly employs the FS-hydrogel as a natural solvent to replace pure water in preparing the electrolyte with 2.0 M $ZnSO_4$ concentration. Due to its superior wettability and multiple hydrophilic and zincophilic functional groups, the FS-based electrolyte provides abundant nucleation sites for Zn, promoting uniform deposition and interfacial stability. Thus, the FS hydrogel serves as a natural solvent, offering effective hydrogen-bond regulation, minimized water activity, and thereby enhanced electrochemical interface stability in a green, sustainable, and scalable electrolyte system. The FS-based electrolyte demonstrated an ultrahigh Zn^{2+} transference number of 0.79, indicating efficient charge transport and reduced concentration polarization. In addition, Zn//Zn symmetric cells employing FS-based electrolyte exhibited remarkable cycling stability, sustaining highly reversible Zn plating/stripping for over 3000 h at 1.0 mA cm^{-2} (1.0 mAh cm^{-2}), 2500 h at 2.0 mA cm^{-2} (2.0 mAh cm^{-2}), and 700 h at 10 mA cm^{-2} (1.0 mAh cm^{-2}). Along with detailed electrochemical and morphological characterizations, the performance of the Zn//V_2O_5 full cell using the FS-based electrolyte is presented in detail.

2 | Results and Discussion

The scheme illustrating the fabrication steps of the FS-based electrolyte is presented in Figure 1a. Commercially available flaxseeds were soaked in deionized (DI) water for 24 h at room temperature and subsequently used for gelation without additional purification. FS-hydrogel was extracted by soaking 1.0, 5.0, and 10.0 g of flaxseeds in 100 mL of DI water, yielding viscous and transparent hydrogels.

To elucidate the chemical composition and identify the functional groups present in FS-hydrogel, it was freeze-dried to obtain the FS aerogel (Figure S1). As shown in Figure 1b, the FTIR spectrum of the FS aerogel displays characteristic bands associated with phenolic acids and disaccharides. A notably broad band at 3413 cm^{-1} is indicative of the O—H stretching vibrations of hydroxyl groups that are engaged in extensive hydrogen bonding among phenolic and carbohydrate species. The subtle peaks

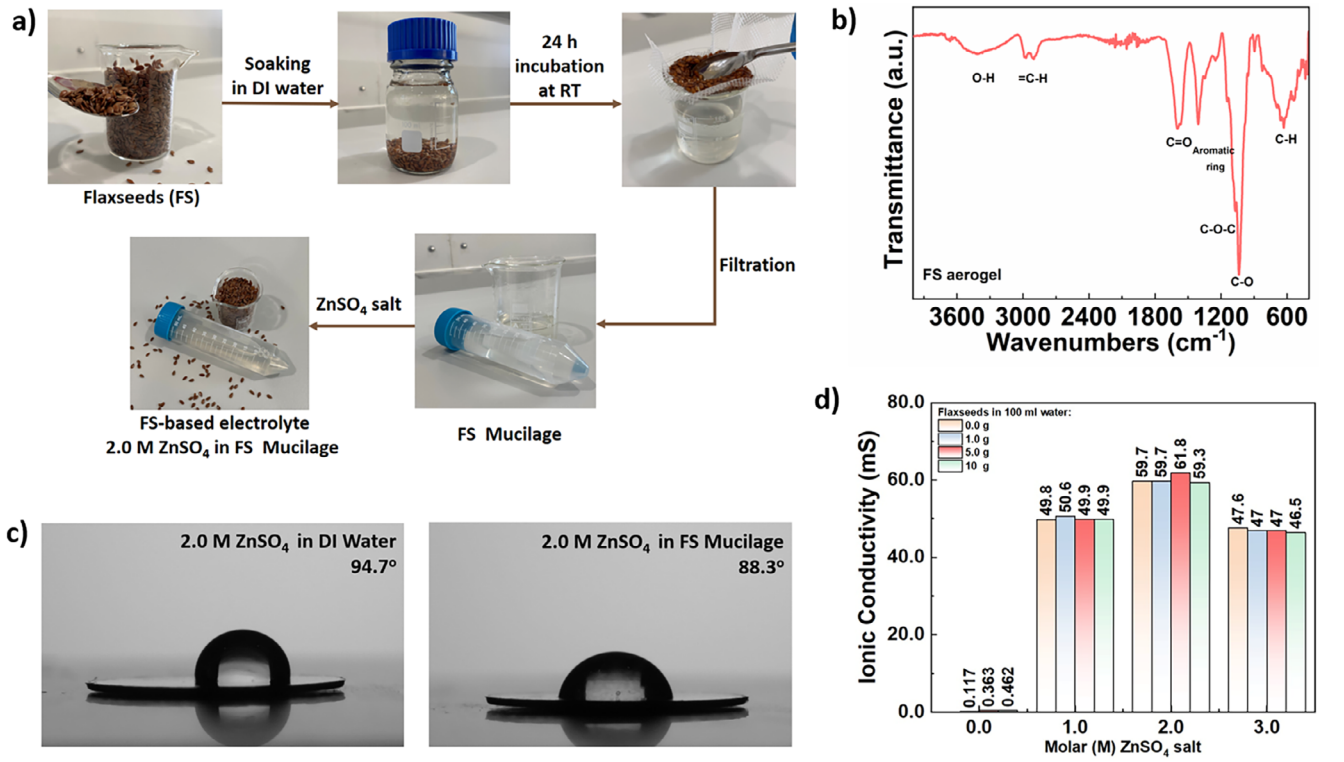

FIGURE 1 | Electrolyte formulation. (a) Schematic of FS-based electrolyte fabrication steps. (b) FTIR spectrum of the FS aerogel. (c) Contact angle measurements on Zn anode surface with aqueous and FS-based electrolytes. (d) Bar graph showing ionic conductivities of the produced electrolytes.

observed at 2983 and 2900 cm^{-1} are linked to the aliphatic C—H stretching vibrations of carbohydrate rings. Distinct bands located at 1598 and 1566 cm^{-1} are attributed to the aromatic C═C stretching vibrations of phenolic compounds, which overlap with the asymmetric stretching of carboxylate (COO^-) groups that arise from deprotonated phenolic acids. The bands at 1407 and 1345 cm^{-1} correspond to the symmetric stretching of carboxylate groups, as well as the C—O/H—O bending vibrations of phenolic hydroxyls and alcohols present in sugars [33, 34]. The pronounced absorptions at 1242, 1140, 1076, and 1038 cm^{-1} are attributed to the C—O—C and C—O stretching vibrations of glycosidic linkages, while the band at 893 cm^{-1} signifies β-type glycosidic configurations. The weak peak at 628 cm^{-1} is associated with the out-of-plane bending of aromatic C—H. Overall, these peaks confirm that the FS-hydrogel consists of hydroxyl- and carbonyl-rich phenolic and sugar molecules that form a hydrogen-bonded molecular network [30].

In metal-based batteries, the superior wettability of electrolytes can reduce nucleation overpotential, enhance the number of nucleation sites, equalize the distribution of cations at the interface, and facilitate the development of thin and stable solid electrolyte interface (SEI) films. This results in the inhibition of dendrite formation, thereby improving the cycle stability and safety of metal-based batteries [35]. The degree of wettability provides insight into the electrolyte–electrode interaction, which critically influences Zn nucleation and corrosion behavior [36]. To evaluate the interfacial wettability and surface affinity between the electrolyte and the Zn anode, contact angle measurements were performed using both aqueous and FS-based electrolytes, as shown in Figure 1c. The contact angle for the aqueous electrolyte was measured at 94.7°. The FS-based electrolyte exhibits a contact angle of 88.3°, indicating improved compatibility between the electrolyte and the electrode. This increase in wettability is a result of the adsorption of hydrophilic phenolic hydroxyl groups and other zincophilic groups on the surface of Zn, promoting a uniform distribution of the electric field and facilitating the development of a dynamic protective layer [37].

The pH of the neat FS-hydrogel prepared from 5.0 g of flaxseeds was measured as 5.62, which decreased to 3.92 after adding 2.0 M $ZnSO_4$. This reduction in pH is attributed to the chelation of Zn^{2+} ions with organic acids and phenolic compounds in the FS mucilage, forming carboxylate and phenoxide coordination complexes that release protons into the medium (Figure S2) [38]. The ionic conductivity of the neat FS-hydrogel was evaluated using an ionic conductivity probe, yielding values of 0.117, 0.363, and 0.467 mS cm^{-1} for mucilages prepared with 1.0, 5.0, and 10.0 g of flaxseeds per 100 mL of deionized water, respectively (Figure 1d). The observed increase in conductivity with higher FS content is attributed to the greater concentration of polar functional groups, such as hydroxyl, carboxyl, and phenolic moieties, that are extracted into the aqueous phase, thereby enhancing proton and ion transport within the hydrogel network. Notably, even in the absence of $ZnSO_4$, the intrinsic ionic conductivity of the FS-hydrogel is sufficient to serve as an aqueous electrolyte medium. However, the incorporation of $ZnSO_4$ salt further improves ionic transport and enables stable and reversible Zn plating/stripping behavior, which is essential for long-term battery operation. Upon the addition of $ZnSO_4$ salt, the gel-like structure of the FS-hydrogel transitioned into a less viscous, more fluid form, indicating disruption of the original hydrogen-bonded network

through coordination interactions between Zn^{2+} ions and the mucilage's functional groups. The FS-based electrolytes prepared with varying concentrations of zinc salt (1.0, 2.0, and 3.0 M $ZnSO_4$) demonstrated both homogeneity and stability, indicating a favorable miscibility of Zn ions within the hydrogel matrix. The ionic conductivity of these FS-electrolytes was measured at room temperature, and the results are provided in Figure 1d. The conductivity values for all formulations ranged from 46.5 to 61.8 mS cm^{-1}. An increase in $ZnSO_4$ concentration from 1.0 to 2.0 M led to a gradual rise in conductivity, peaking at 61.8 mS cm^{-1}. However, when concentrations exceeded 2.0 M, a decline in conductivity was observed, suggesting a competition between increased ion density and reduced mobility due to ion–ion interactions and partial coordination between Zn^{2+} ions and the polar hydrophilic organic molecules within the FS-based electrolyte. This finding is in line with previous studies on concentrated aqueous electrolytes, which have shown that although ionic conductivity initially increases with salt concentration, it eventually decreases at higher concentrations due to enhanced ion–ion interactions and the formation of ion pairs or aggregates that reduce ion mobility and the number of freely mobile charge carriers [39–41]. Consequently, the FS-based electrolyte having 2.0 M $ZnSO_4$ was chosen as the optimum electrolyte for this study and used throughout the electrochemical characterization of the new electrolyte.

To explore the capability of the FS-based electrolyte in mitigating HER activity and enhancing the interfacial stability of the Zn anode, a comprehensive series of electrochemical tests was conducted, providing a detailed understanding of the electrolyte's effect on electrochemical processes. Linear sweep voltammetry (LSV) was employed to evaluate the electrochemical stability window (ESW) of the FS-based electrolyte and to assess its hydrogen evolution reaction (HER) behavior. As shown in Figure 2a, when the potential reaches −0.19 V, the cathodic current density of the Zn anode in contact with the FS-based electrolyte (−24.98 mA cm^{-2}) is lower than that of the Zn anode in contact with the aqueous electrolyte (−26.69 mA cm^{-2}). The reduced cathodic current indicates suppressed hydrogen evolution in the cell employing the FS-based electrolyte [21].

Tafel plots were used to evaluate the corrosion current (I_{corr}) and the corrosion potential (E_{corr}), as shown in Figure 2b. The FS-based electrolyte showed a notably reduced I_{corr} (0.978 mA cm^{-2}) and an increased E_{corr} (-0.89 V vs Ag/AgCl) in comparison to the aqueous electrolyte (I_{corr} = −1.426 mA cm^{-2}, E_{corr} = −0.90 V vs Ag/AgCl). The higher E_{corr} and lower I_{corr} values suggest a diminished corrosion on the anode surface [42]. The corrosion inhibition efficiency (η) was also calculated using the I_{corr} values of the fabricated electrolytes, and the % η is calculated as 31.4%. Thus, the findings reveal that the use of FS-based electrolytes significantly lowers the HER activity and the anodic corrosion of the Zn anode.

Cyclic voltammetry (CV) tests were done using asymmetric Zn//Cu cells to investigate Zn^{2+} nucleation overpotential on the Zn anode. As shown in Figure 2c, both aqueous and FS-based electrolytes exhibit distinct and reversible redox peaks corresponding to Zn plating/stripping processes, confirming their electrochemical reversibility. In the CV curves, the turning point during the cathodic scan marks the onset of Zn^{2+} nucleation, with the associated potential representing the nucleation overpotential (NOP). The FS-based electrolyte produced a higher current density, reflecting its enhanced Zn^{2+} kinetics relative to the aqueous electrolyte. The nucleation overpotential of the FS-based system (−53.6 mV) is lower than that of the aqueous electrolyte (−64.8 mV), indicating a reduced Zn deposition barrier and facilitated plating/stripping behavior [43]. Further evaluation at 0.1 mA cm^{-2} (Figure 2d) showed a decrease in NOP from 11.67 mV in the aqueous electrolyte to 9.08 mV in the FS-based system. The lower overpotential, attributed to weaker Zn^{2+} solvation, underscores the efficacy of FS-hydrogel in facilitating uniform Zn nucleation while suppressing H_2O reduction [44].

The Zn ion transference number ($t_{Zn^{2+}}$) serves as a vital parameter that determines the distribution of Zn^{2+} ions at the interface between the anode and electrolyte, which impacts the efficiency of Zn metal batteries. The $t_{Zn^{2+}}$ for the FS-based electrolyte was determined using symmetric cells with Zn anodes. The corresponding I-t curve and EIS spectra, observed before and after the polarization process, are shown in Figure 2e. The $t_{Zn^{2+}}$ was calculated to be 0.79, but $t_{Zn^{2+}}$ value of the aqueous $ZnSO_4$ was found to be 0.32 (Figure S3). The high $t_{Zn^{2+}}$ reflects the FS-based electrolyte's ability to regulate Zn^{2+} ion flux, improving electrochemical performance by minimizing side reactions and controlling Zn deposition, which is linked to the rich availability of −OH, glycosidic ether (C—O—C) and carboxylate (—O—C═O) groups within FS-based electrolyte, as well as the hydrogen bonding network that modulates the solvation structure of the electrolyte [9, 17, 45].

Temperature-dependent electrochemical impedance spectroscopy (EIS) was conducted to elucidate the temperature effect on the interfacial charge transfer behavior of Zn//Zn symmetric cells using both aqueous and FS-based electrolytes. As shown in Figure 2f (Figure S4 for aqueous electrolyte), the Nyquist plots exhibit a clear trend of decreasing semicircle diameter with increasing temperature for both electrolytes, indicating a reduction in charge-transfer resistance (R_{ct}) at elevated temperatures. The relationship between temperature and R_{ct} was further analyzed using the Arrhenius equation. The corresponding Arrhenius plots (Figure S5) reveal linear correlations, from which the activation energies were calculated to be 24.70 and 36.86 kJ mol^{-1} for the aqueous and FS-based electrolytes, respectively. This finding was also supported by the lower Zn^{2+} diffusion coefficient with the FS-based electrolyte (Figure S6). The higher value of the FS-based electrolyte reflects a more structured solvation environment and stronger coordination between Zn^{2+} ions and the functional groups (—OH, —COOH, and C—O—C) in the FS-hydrogel matrix. Such strong interactions and the presence of a hydrogen-bonded network hinder ion mobility to a certain extent, requiring higher energy for charge transfer. Nevertheless, this feature is beneficial for stabilizing Zn deposition by suppressing parasitic reactions and uncontrolled dendritic growth, thus maintaining interfacial integrity during prolonged cycling.

The effectiveness of the FS-based electrolyte in enhancing the electrochemical stability of Zn anodes was examined through long-term galvanostatic cycling of symmetric Zn//Zn cells operated under varied current densities and areal capacities. For comparison, stability results for the symmetric cells with the

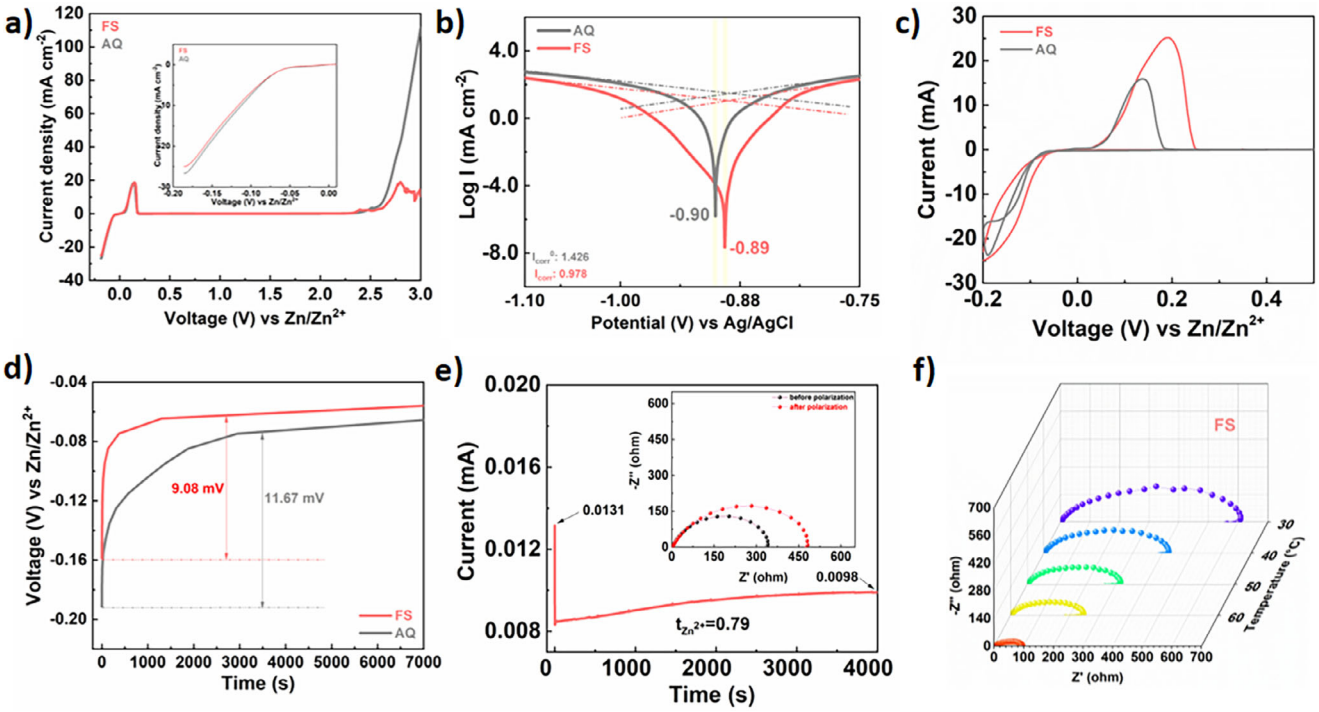

FIGURE 2 | (a) LSV curves and (b) Tafel plots of aqueous and FS-based electrolytes at a scan rate of 1.0 mV s^{-1}. (c) CV curves of aqueous and FS-based electrolyte in Zn//Cu cells at 1.0 mV s^{-1}. (d) Nucleation overpotential curves. (e) Chronoamperometry and EIS curves of FS-based electrolyte before and after dc polarization. (f) Temperature-dependent EIS spectra of symmetrical Zn//Zn cell using FS-based electrolyte.

aqueous electrolyte cycled under the same conditions were also provided. Galvanostatic charge–discharge (GCD) curves of the symmetrical cells are provided in Figure 3. In Figure 3a, at a current density of 1.0 mA cm^{-2} and an areal capacity of 1.0 mAh cm^{-2}, the symmetric cell containing the FS-based electrolyte demonstrated impressively stable cycling performance and operated for over 3000 h. It should be noted that, in a two-electrode Zn//Zn symmetric configuration, the measured overpotential reflects the combined contributions of Zn plating and Zn stripping at both electrodes; therefore, transient voltage fluctuations are intrinsic to this testing method and do not necessarily indicate interfacial instability. The overpotential fluctuation for the FS-based electrolyte was slightly higher (~59 mV) than that observed in the aqueous electrolyte (~44 mV) for the initial cycles. After approximately the 86th cycle, the overpotential fluctuation for the FS-based electrolyte was around 100 mV. In contrast, the symmetric cells employing the aqueous electrolyte exhibited a sudden voltage drop after approximately 235 h of cycling, indicative of a short circuit. The electrochemical stability tests were further extended to higher current densities and areal capacities to examine the compatibility of the FS-based electrolyte under challenging operating conditions. Figure 3b shows the cycling stability of the symmetric cells cycled at 2.0 mA cm^{-2} (2.0 mAh cm^{-2}). The symmetric cell containing the aqueous $ZnSO_4$ electrolyte experienced an early short circuit and cell failure after only 56 cycles (112 h), highlighting its poor interfacial stability. In contrast, the cell with the FS-based electrolyte demonstrated remarkable long-term electrochemical stability, sustaining excellent cyclic stability for over 2500 h. During the initial 80 h, the FS-based electrolyte maintained a low overpotential of approximately 50 mV, which gradually stabilized at around 100 mV with minimal fluctuation throughout prolonged cycling. For 2500 h of cycling, the cell remained stable, confirming that the FS-based electrolyte effectively suppressed parasitic side reactions and ensured highly reversible Zn plating/stripping. At a high current density of 5.0 mA cm^{-2} (5.0 mAh cm^{-2}), the cell with the aqueous electrolyte exhibited a slightly lower overpotential (~58 mV) and failed after only 68 cycles (136 h). In contrast, the FS-based electrolyte cell maintained excellent electrochemical stability with an overpotential of ~62.5 mV, sustaining stable cycling for up to 236 h (Figure 3c). Electrochemical stability measurements were continued at highly challenging conditions, which is an important prerequisite for high-power applications. When the current density is increased to 10 mA cm^{-2} (10 mAh cm^{-2}), the aqueous electrolyte-containing cell exhibited poor cycling stability and experienced a rapid short circuit just after 47 cycles (95 h), as presented in Figure 3d. On the other hand, the FS-based electrolyte cell maintained its stable operation for over 600 h under the extremely high current density, demonstrating a highly reversible and stable Zn plating/stripping process. Remarkably, a minor change in overpotential at high current densities is likely due to the formation of a compact and uniform Zn layer, which promotes efficient charge transfer and minimizes polarization at the anode interface [45]. The electrochemical stability tests were further conducted under incrementally varied current densities. The current density was gradually increased from 1.0 to 10 mA cm^{-2} (1.0–10 mAh cm^{-2}) over 200 h intervals, and subsequently decreased following the same sequence as depicted in Figure 3e. The aqueous electrolyte cell failed after 380 hours and could not complete the analysis due to dendrite formation, whereas the FS-based cell exhibited outstanding stability, maintaining an almost constant overpotential throughout the entire cycling process beyond 800 h. The beneficial effect of incorporating

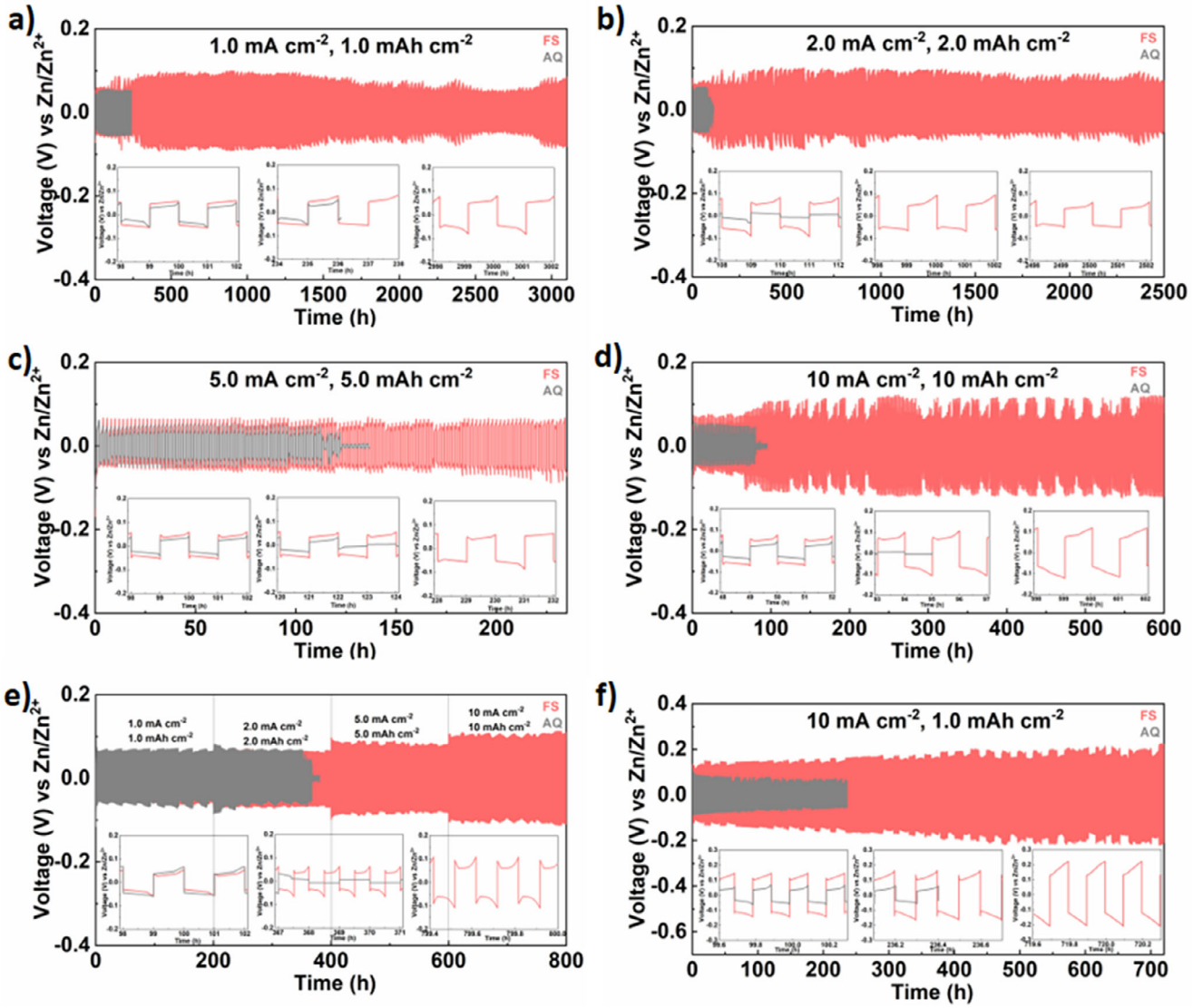

FIGURE 3 | Electrochemical stability tests. Galvanostatic charge discharge (GCD) curves of symmetrical Zn//Zn cells with aqueous and FS-based electrolytes at different current densities and areal capacities: of (a) 1.0 mA cm^{-2}, 1.0 mAh cm^{-2}, (b) 2.0 mA cm^{-2}, 2.0 mAh cm^{-2}, (c) 5.0 mA cm^{-2}, 5.0 mAh cm^{-2}, and (d) 10.0 mA cm^{-2}, 10.0 mAh cm^{-2}. (e) Rate performance comparison of Zn//Zn cells with aqueous and FS-based electrolytes at various current densities ranging from 1.0 to 10 mA cm^{-2} (1.0–10 mAh cm^{-2}). (f) Cycling stability of Zn//Zn cells cycled at 10 mA cm^{-2} with a fixed capacity of 1.0 mAh cm^{-2}.

FS-based gel in reducing water activity and mitigating side reactions becomes particularly evident under high current density conditions (10 mA cm^{-2}) with a plating capacity of 1.0 mAh cm^{-2} [46, 47]. As shown in Figure 3f, the cell with the aqueous electrolyte exhibited poor cycling stability and experienced a short circuit after only 236 h. In contrast, the FS-based electrolyte cell maintained stable operation for 720 h under the same high current density. Coulombic efficiency (CE) measurements of the asymmetric Zn//Cu cells were presented in Figure S7. Overall, the obtained stability results demonstrate that the FS-based electrolyte effectively regulates Zn^{2+} ion flux and suppresses dendritic growth, leading to a more stable anode/electrolyte interface and enhanced long-term cycling reversibility. This improvement stems from the reduced water activity and strong Zn^{2+} coordination enabled by the rich functional groups of FS-hydrogel, which collectively promote uniform Zn deposition and inhibit unwanted side reactions during extended cycling. Within the electrolyte, polar functional groups coordinate with Zn^{2+} ions, regulating the solvation structure and acting as hydrogen bond donors and acceptors (HBD/HBA), thereby influencing the hydrogen bonding structure. This hydrogen-bond network confines free water molecules, thereby lowering their activity and reshaping the Zn^{2+} solvation sheath, which in turn mitigates parasitic side reactions [48]. Table S1 presents a comparison of the electrochemical stability of the FS-based electrolyte developed in this study with notable aqueous ZIB electrolytes that incorporate natural additives, as reported in the literature. The remarkable electrochemical stability of FS-based electrolyte underscores its strong potential as a sustainable and cost-effective electrolyte for advanced Zn-based energy storage systems.

To further investigate the Zn deposition behavior in FS-based electrolytes, structural and morphological analyses were performed on the cycled Zn anodes. For this purpose, ex situ SEM

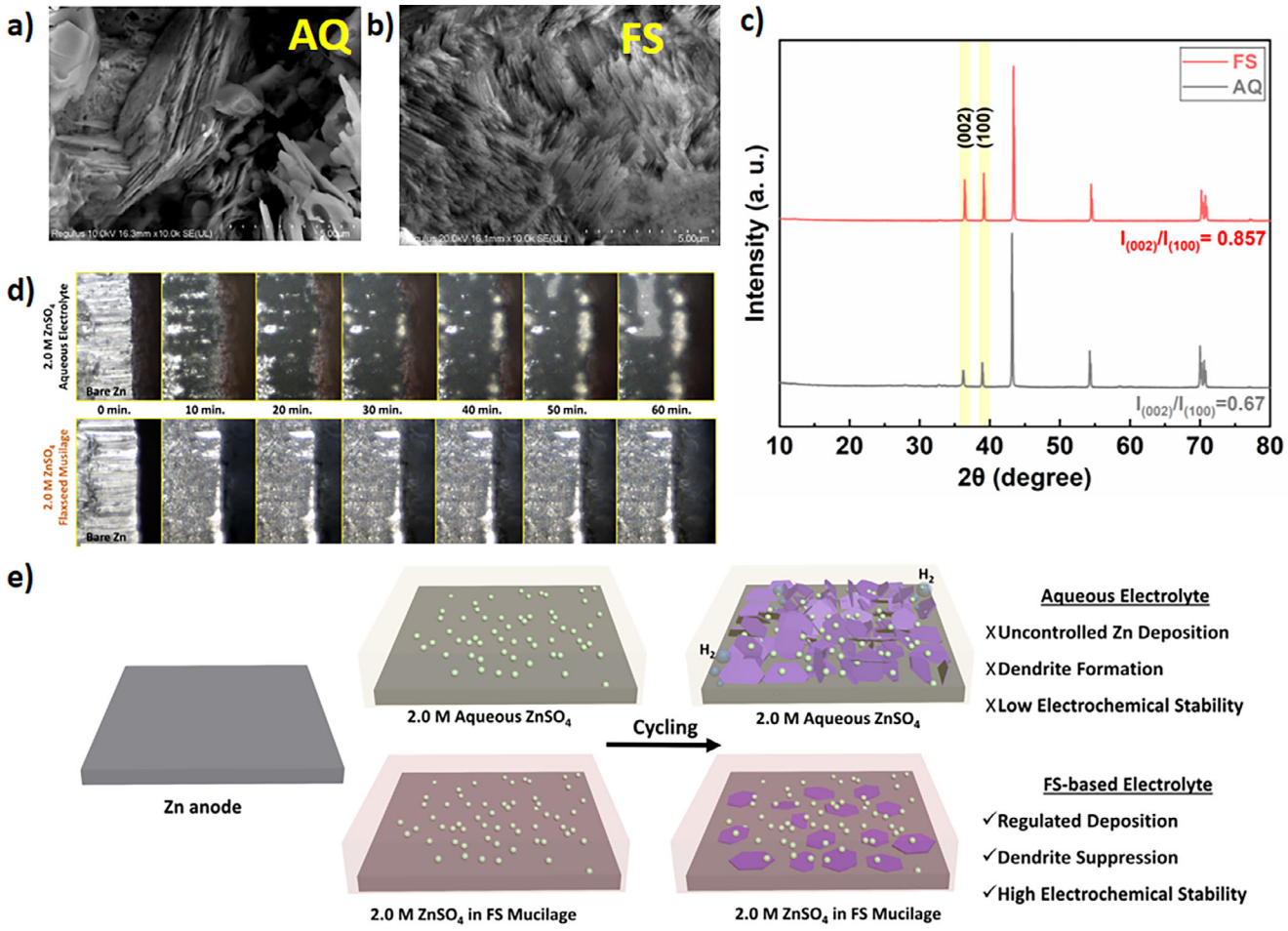

FIGURE 4 | Ex situ SEM images of cycled Zn anodes in (a) aqueous and (b) FS-based electrolytes. (c) Ex situ XRD patterns of the cycled Zn anodes. (d) In-operando optical microscopy images of Zn anodes in the electrolyte solutions. (e) Schematics of Zn deposition behavior on Zn anodes in aqueous and FS-based electrolytes.

analysis was conducted on the cycled Zn anodes after the cycling. Ex situ SEM images of the cycled Zn anodes in the aqueous and FS-based electrolytes are presented in Figure 4a,b, respectively. After cycling, the Zn anode subjected to the aqueous electrolyte demonstrated significant, multidirectional dendritic growths and hexagonal flake-like deposits, suggesting pronounced interfacial instability and irregular Zn nucleation throughout the repeated cycling. On the other hand, the Zn anode cycled in the FS-based electrolyte exhibited a smooth, highly compact, and morphologically uniform surface, indicating uniform Zn deposition and stable Zn stripping/plating characteristics.

Ex situ X-ray diffraction (XRD) analysis was performed on the cycled Zn anodes to elucidate the electrochemical interactions between the exposed Zn crystal planes and the electrolyte at the electrode–electrolyte interface. As shown in Figure 4c, the ex situ XRD patterns of the cycled Zn anodes from both the FS-based and aqueous electrolytes exclusively display diffraction peaks associated with metallic Zn. Specifically, the cycled Zn anode from the Zn||Zn cell employing the FS-based electrolyte exhibits diffraction peaks at 36.43°, 39.29°, 43.35°, and 54.43°, along with weak reflections at 70.20° and 70.75°, which can be indexed to the (002), (100), (101), (102), (103), and (110) planes of hexagonal Zn (JCPDS No. 04–0831), respectively, confirming the formation of crystalline Zn after cycling. Compared with the aqueous electrolyte, the FS-based electrolyte shows higher relative intensities of the (002) and (101) reflections, suggesting an enhanced contribution of these crystallographic planes during Zn deposition. Furthermore, the relative intensity ratio of the (002) and (100) peaks (I(002)/I(100)) provides insight into the preferential deposition behavior of Zn. As depicted in Figure 4c, the I(002)/I(100) ratios are 0.670 and 0.857 for the cycled Zn anodes in the aqueous and FS-based electrolytes, respectively. A higher I(002)/I(100) ratio is indicative of preferential Zn deposition along the basal plane [9]. Accordingly, the increased I(002)/I(100) ratio demonstrates an enhancement of Zn nucleation along the (002) crystal plane in the FS-based electrolyte compared with the aqueous electrolyte.

These ex-situ results for the cycled Zn anodes in both electrolytes further validate that the electrolyte employing FS-hydrogel as the natural solvent effectively regulates the flux of Zn^{2+} ions and inhibits dendritic growth, enhancing the electrochemical stability of the Zn anodes.

To closely monitor the Zn plating behavior and the associated HER activity, in-operando optical microscopy analysis was performed. For the analysis, Zn plating was performed at a current

density of 5.0 mA cm^{-2} for a 60-min duration. As shown in Figure 4d, the Zn anode retained a smooth and compact surface with no visible dendrite formation in the FS-based electrolyte. In contrast, the aqueous electrolyte exhibited noticeable dendritic growth on the Zn surface within 10 min, which progressively evolved into irregular and enlarged dendrites after 60 min of plating.

Figure 4e schematically illustrates the Zn deposition behavior on Zn anodes in aqueous and FS-based electrolytes, consistent with the ex situ SEM and XRD results. The aqueous electrolyte promotes nonuniform Zn deposition and random crystal growth, leading to a dendritic morphology and dominant growth along the Zn(100) plane, as evidenced by ex situ XRD and SEM results. In contrast, the FS-based electrolyte promotes dense and uniform Zn deposition with a preferred Zn(002) orientation, consistent with the smooth, dendrite-free surface observed via ex-situ SEM and XRD analysis.

The electrochemical performance of the fabricated FS-based electrolyte was investigated in a full ZIB device architecture using vanadium (V) oxide nanowires (V_2O_5 NWs) as cathode material. The structural and morphological characterizations of the V_2O_5 NWs are provided in the Figures S8–S10. The CV curves of the ZIBs using FS-based and aqueous electrolytes, recorded at a scan rate of 0.5 mV s^{-1} within a voltage window of 0.2–1.6 V, exhibited two distinct pairs of oxidation and reduction peaks associated with the V_2O_5 cathode (Figure 5a). The use of FS-based electrolyte does not alter the redox behavior of the V_2O_5 cathode. During the CV scan, two oxidation peaks are observed sequentially at approximately 0.771 and 1.252 V, which are associated with the transition processes of V^{4+}/V^{5+} and V^{3+}/V^{4+}. Also, two reduction peaks are sequentially observed at around 0.732 and 0.384 V, corresponding to the reduction processes of V^{5+}/V^{4+} and V^{4+}/V^{3+}. The CV profile of the full cell in the aqueous electrolyte displayed analogous redox peaks at 0.836/0.476 V and 1.274/0.728 V. The oxidation peak observed at 1.252 V experienced a minor shift (~22 mV) towards a lower potential in comparison to the aqueous electrolyte. Unlike the FS-based electrolyte, which exhibited a greater integral area in the CV curves, indicating an enhanced Zn^{2+} storage capacity. It is noteworthy that the FS-based electrolyte shows considerable enhancement in oxidation-reduction peaks, indicating that the FS-hydrogel, as a natural solvent, improves the ion-storage ability of the V_2O_5 cathode.

The CV measurements were repeated at scan rates ranging from 0.1 to 1.0 mV s^{-1} to evaluate the rate-dependent electrochemical behavior of the electrolytes (Figure 5b and Figure S11). As the scan rate increased, the oxidation peaks shifted towards higher voltages, whereas the reduction peaks shifted towards lower voltage values. Both the redox peak current density and the peak-to-peak separation increased in both electrolytes, which can be attributed to the rapid charge polarization at the electrode surface under faster potential sweep conditions. To determine the charge storage mechanisms of the fabricated electrolyte solutions, the contributions from surface-capacitive components were visualized utilizing the CV curves at different scan rates (Figures S12 and S13). Additionally, b-values were calculated to quantify the roles of diffusion control and surface capacitance in the charge storage mechanisms of ZIBs. As illustrated in Figure 5g, the b-values for peaks O1, O2, R1, and R2 were calculated to be 0.801, 0.912, 0.817, and 0.784, respectively, for the cell using a FS-based electrolyte (Figure S14 for aqueous electrolyte). The obtained values indicate that both diffusive and surface-capacitive processes govern the charge-storage process.

The impact of replacing the water with FS-hydrogel on the electrochemical performance of the ZIBs was further evaluated through electrochemical impedance spectroscopy (EIS). The series resistance (R_s) values for the fabricated ZIB cells using the FS-based and aqueous electrolytes were found to be 1.54 and 2.83 Ω, respectively. The R_{ct} values, obtained from the semicircles in the high frequency regions of the Nyquist plots, were 103.2 Ω for the FS-based electrolyte and 619.7 Ω for the aqueous electrolyte (Figure 5d). The significantly reduced R_{ct} by the FS-based electrolyte demonstrates that the FS-hydrogel effectively reduces water activity and suppresses the formation of corrosion-induced byproducts, thereby lowering HER activity and maintaining a more conductive Zn surface. In contrast, the aqueous electrolyte promotes parasitic reactions such as HER activity and surface corrosion, resulting in increased R_{ct} due to the formation of insulating byproducts. The prevention of undesired side reactions can substantially lower surface passivation [2], which in turn enhances the charge transfer process, as indicated by the reduction in charge transfer resistance [45]. Consequently, the FS-based electrolyte enables faster interfacial charge transfer and enhanced Zn plating/stripping kinetics.

To evaluate the effect of the FS-based electrolyte on the electrochemical performance of ZIBs, GCD measurements were conducted across current densities ranging from 0.2 to 10 A g^{-1}. As shown in Figure 5e, at 0.2 A g^{-1}, the full ZIB cell employing the FS-based electrolyte delivered a specific capacity of 233.8 mAh g^{-1}, outperforming the 210.4 mAh g^{-1} obtained with the aqueous $ZnSO_4$ electrolyte. In addition, the FS-based cell exhibited a lower voltage hysteresis (199 mV) compared to the aqueous electrolyte (237 mV), indicating improved Zn^{2+} reaction kinetics. GCD measurements were repeated at different current densities, and the FS-based electrolyte delivered higher specific capacities than the aqueous electrolyte at every current density (Figure 5f and Figure S15). The current density vs. specific capacity results are provided in Figure 5g. As shown in Figure 5g, the FS-based cell maintained a high specific capacity profile at all current densities, whereas the cell using the aqueous electrolyte exhibited noticeably lower capacity values. Moreover, the capacity recovery of the FS-based ZIB from 10 A g^{-1} back to 0.2 A g^{-1} was markedly better than that of the aqueous electrolyte cell, highlighting its superior rate capability and reversibility. The electrochemical performance of the FS-based electrolyte was further benchmarked against previously reported ZIBs employing vanadium-based cathodes and aqueous electrolytes, as presented in Table S2.

The long-term cycle life and capacity retention of the full ZIB cells, which utilize FS-based and aqueous electrolytes, were also examined. At a current density of 1.0 A g^{-1} (Figure 5h), the Zn//V_2O_5 cell containing the FS-based electrolyte delivered a markedly higher initial discharge capacity of 321.9 mAh g^{-1}, compared to 307.5 mAh g^{-1} for the cell using the aqueous electrolyte. After 1000 cycles, the FS-based electrolyte retained 102.5 mAh g^{-1}, while the aqueous electrolyte using cell declined to 73.4 mAh g^{-1}, highlighting a clear advantage in capacity

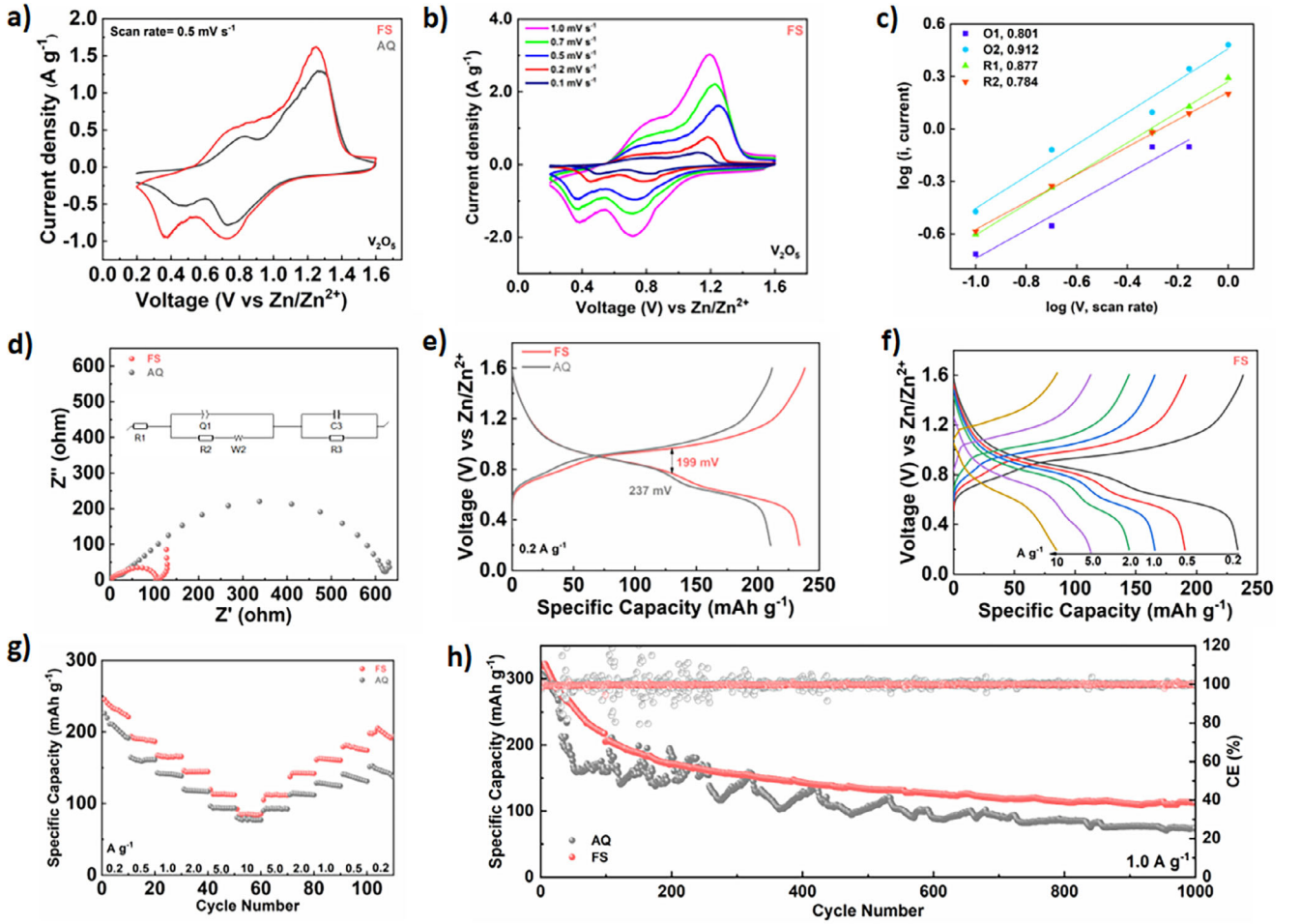

FIGURE 5 | Electrochemical performance of the full ZIB cells with V_2O_5 NW cathodes in 2.0 M $ZnSO_4$ aqueous and FS-based electrolytes. (a) Comparison of CV profiles at a scan rate of 0.5 mV s^{-1}. (b) CV curves of ZIB using FS-based electrolyte at various scan rates. (c) The linear fitting plots corresponding to the logarithm of current against the logarithm of scan rate for both anodic and cathodic peaks. (d) Nyquist plots (inset: equivalent circuit model). (e) Comparison of GCD curves at 0.2 A g^{-1} current density. (f) GCD curves of the ZIB cell using FS-based electrolyte across varying current densities. (g) The rate performance in different electrolytes. (h) Comparison of long-term GCD cycling performance of aqueous and FS-based electrolytes at 1.0 A g^{-1}.

retention. The remarkable durability of the FS-based electrolyte is attributed to the suppressed electrochemical corrosion and the absence of dendritic accumulation on the Zn anode [49]. Furthermore, inhibiting the side reactions occurring at both the anode and cathode can significantly diminish surface passivation caused by the accumulation of byproducts, thereby facilitating the charge transfer process, as evidenced by the decreased charge transfer resistance [45].

The gradual capacity decay observed during long-term cycling of the Zn//V_2O_5 full cell (Figure 5h) is primarily attributed to intrinsic limitations of the V_2O_5 cathode rather than instability of the Zn anode. Vanadium-based cathodes are prone to structural distortion and partial dissolution of vanadium species in mildly acidic aqueous electrolytes during repeated Zn^{2+} insertion/extraction, leading to progressive loss of active material and capacity fading upon prolonged cycling (Figure S16). In addition, slow electrolyte consumption and interfacial reorganization within the FS-based hydrogel matrix may contribute to a moderate increase in interfacial resistance at extended cycle numbers, slightly restricting Zn^{2+} transport kinetics. Nevertheless, Zn anode-related degradation is effectively suppressed in the FS-based electrolyte, as evidenced by the long-term stability of Zn//Zn symmetric cells, high Zn^{2+} transference number (0.79), reduced corrosion current density, suppressed HER activity, and dendrite-free Zn morphology after cycling. These results indicate that the FS-based electrolyte significantly mitigates anode-induced degradation, and the remaining capacity decay in the full cell is predominantly governed by cathode-side structural and chemical evolution rather than Zn anode failure or severe impedance growth.

3 | Conclusions

In summary, unlike previously reported biomass-derived additives that require the precise blending of synthetic organic molecules into aqueous electrolytes, we formulated the FS-based electrolyte using the flaxseed hydrogel without any purification or chemical modification. This approach offers a simpler, greener, and more scalable electrolyte formulation strategy, eliminating the need for industrially processed or synthetic organic compounds as additives. Due to its superior wettability, the

FS-based electrolyte system features multiple polar hydrophilic and zincophilic functional groups, which create abundant nucleation sites for Zn and regulate the hydrogen-bond network. Consequently, the FS-based electrolyte promotes dense and uniform Zn deposition with a preferred Zn(002) orientation. The FS-based electrolyte exhibited remarkable t_{Zn}^{2+} of 0.79 and superior electrochemical stability for symmetric Zn//Zn cells, sustaining electrochemical stability for 3000 h at a current density of 1.0 mA cm^{-2} (1.0 mAh cm^{-2}). The Zn//V_2O_5 full cells assembled with the FS-based electrolyte demonstrated superior specific capacities, improved rate capability, and significantly greater capacity retention compared to aqueous electrolytes, highlighting its substantial role in enhancing the performance of Zn-based batteries. Overall, this study presents a straightforward design for biomass electrolytes that advances the sustainable development of safe and durable Zn-ion batteries.

Conflicts of Interest

The authors declare no conflicts of interest.

Data Availability Statement

The data that support the findings of this study are available from the corresponding author upon reasonable request.

References

1. X. Zhang, Y. Liu, S. Wang, et al., "Fundamentals and Design Strategies of Electrolytes for High-temperature Zinc-ion Batteries," *Energy Storage Materials* 70 (2024): 103471, https://doi.org/10.1016/j.ensm.2024.103471.

2. J. Hao, X. Li, X. Zeng, D. Li, J. Mao, and Z. Guo, "Deeply Understanding the Zn Anode Behaviour and Corresponding Improvement Strategies in Different Aqueous Zn-based Batteries," *Energy & Environmental Science* 13 (2020): 3917–3949, https://doi.org/10.1039/D0EE02162H.

3. J. Zhu, Z. Tie, S. Bi, and Z. Niu, "Towards More Sustainable Aqueous Zinc-Ion Batteries," *Angewandte Chemie International Edition* 136 (2024): 202403712.

4. W. Chen, S. Guo, L. Qin, et al., "Hydrogen Bond-Functionalized Massive Solvation Modules Stabilizing Bilateral Interfaces," *Advanced Functional Materials* 32 (2022): 2112609.

5. S. Gao, Z. Zhang, F. Mao, P. Liu, and Z. Zhou, "Advances and Strategies of Electrolyte Regulation in Zn-ion Batteries," *Materials Chemistry Frontiers* 7 (2023): 3232–3258, https://doi.org/10.1039/D3QM00104K.

6. J. Hao, X. Li, S. Zhang, et al., "Designing Dendrite-Free Zinc Anodes for Advanced Aqueous Zinc Batteries," *Advanced Functional Materials* 30 (2020): 2001263, https://doi.org/10.1002/adfm.202001263.

7. J. Zhou, Q. Li, X. Hu, et al., "Water Molecules Regulation for Reversible Zn Anode in Aqueous Zinc Ion Battery: Mini-Review," *Chinese Chemical Letters* 35 (2024): 109143.

8. S. Liu, J. Mao, W. K. Pang, et al., "Tuning the Electrolyte Solvation Structure to Suppress Cathode Dissolution, Water Reactivity, and Zn Dendrite Growth in Zinc-Ion Batteries," *Advanced Functional Materials* 31 (2021): 2104281, https://doi.org/10.1002/adfm.202104281.

9. Z. Xiao, X. Dai, J. Zhu, et al., "Hydrogen Bond Competition Optimizing Aqueous Zn Ion Solvation and (002) Interfacial Deposition With Ultralong Stability," *Advanced Functional Materials* 35 (2025): 2424860, https://doi.org/10.1002/adfm.202424860.

10. K. Zhao, G. Fan, J. Liu, et al., "Boosting the Kinetics and Stability of Zn Anodes in Aqueous Electrolytes With Supramolecular Cyclodextrin Additives," *Journal of the American Chemical Society* 144 (2022): 11129–11137, https://doi.org/10.1021/jacs.2c00551.

11. W. Guo, T. Hua, C. Qiao, Y. Zou, Y. Wang, and J. Sun, "Biomass-based Electrolyte Design for Aqueous Zinc-ion Batteries: Recent Advances and Future Outlook," *Energy Storage Materials* 66 (2024): 103244, https://doi.org/10.1016/j.ensm.2024.103244.

12. G. Yaman Uzunoglu and R. Yuksel, "Toward Green and Sustainable Zinc-Ion Batteries: The Potential of Natural Solvent-Based Electrolytes," *Small* 21 (2025): 2411478, https://doi.org/10.1002/smll.202411478.

13. X. Yang, X. Nie, C. Tang, et al., "Biomass Materials for Zinc-based Sustainable and Green Energy Storage Devices: Strategy and Mechanism," *Nano Research* 18 (2025): 94907031, https://doi.org/10.26599/NR.2025.94907031.

14. L. Wang, H. Shen, W. Sun, et al., "Harnessing Eco-friendly Additives to Manipulate Zinc-ion Solvation Structures towards Stable Zinc Metal Batteries," *Journal of Energy Chemistry* 98 (2024): 114–122, https://doi.org/10.1016/j.jechem.2024.06.029.

15. Q. Sun, H.-H. Du, T.-J. Sun, et al., "Sorbitol-electrolyte-additive Based Reversible Zinc Electrochemistry," *Journal of Electrochemistry* 30, no. 2 (2024).

16. Y. L. Chen, W. W. Yan, Y. F. Yuan, et al., "D-Lactitol Restructures Thick Inner Helmholtz Plane and Coordinates Multi-Zn^{2+} Solvation Sheath via Unique Adsorption Geometry and Super-multi Zincophilic/Hydrophilic Sites," *Journal of Energy Storage* 133 (2025): 118102, https://doi.org/10.1016/j.est.2025.118102.

17. H. Wang, M. Zhu, H. Wang, et al., "Rearrangement of H-bonds Network of Solvation Structure via a Zincophilic Polyol-type Surfactant to Stabilize Zinc Anode in Aqueous Zinc-ion Batteries," *Energy Storage Materials* 67 (2024): 103238, https://doi.org/10.1016/j.ensm.2024.103238.

18. Y. Shang, P. Kumar, T. Musso, et al., "Long-Life Zn Anode Enabled by Low Volume Concentration of a Benign Electrolyte Additive," *Advanced Functional Materials* 32 (2022): 2200606, https://doi.org/10.1002/adfm.202200606.

19. H. Liu, Z. Xin, B. Cao, et al., "Polyhydroxylated Organic Molecular Additives for Durable Aqueous Zinc Battery," *Advanced Functional Materials* 34 (2024): 2309840, https://doi.org/10.1002/adfm.202309840.

20. S. Dilwale, P. P. Puthiyaveetil, A. Babu, and S. Kurungot, "Phytic Acid Customized Hydrogel Polymer Electrolyte and Prussian Blue Analogue Cathode Material for Rechargeable Zinc Metal Hydrogel Batteries," *Small* 20 (2024): 2311923, https://doi.org/10.1002/smll.202311923.

21. P.-F. Zhang, Z. Wu, S.-J. Zhang, et al., "Tannin acid induced anti-corrosive film toward stable Zn-ion batteries," *Nano Energy* 102 (2022): 107721.

22. J. Cao, D. Zhang, R. Chanajaree, et al., "Highly Reversible Zn Metal Anode With Low Voltage Hysteresis Enabled by Tannic Acid Chemistry," *ACS Applied Materials & Interfaces* 15 (2023): 45045–45054, https://doi.org/10.1021/acsami.3c10773.

23. R. Yuksel, "Aloe Vera-Based Green and Sustainable Electrolyte for Zinc Ion Batteries," *Advanced Sustainable Systems* 8 (2024): 2400396, https://doi.org/10.1002/adsu.202400396.

24. M. Kučka, Ľ. Harenčár, K. Ražná, et al., "Great Potential of Flaxseed Mucilage," *European Food Research and Technology* 250 (2024): 877–893.

25. A. Mueed, S. Shibli, S. A. Korma, P. Madjirebaye, T. Esatbeyoglu, and Z. Deng, "Flaxseed Bioactive Compounds: Chemical Composition, Functional Properties, Food Applications and Health Benefits-Related Gut Microbes," *Foods* 11 (2022): 3307.

26. M. T. Haseeb, G. Muhammad, M. A. Hussain, S. N. A. Bukhari, and F. A. Sheikh, "Flaxseed (Linum usitatissimum) mucilage: A versatile stimuli–responsive functional biomaterial for pharmaceuticals and healthcare," *International Journal of Biological Macromolecules* 278 (2024): 134817, https://doi.org/10.1016/j.ijbiomac.2024.134817.

27. O. Barbary, S. Al-Sohaimy, M. El-Saadani, and A. Zeitoun, "Extraction, Composition and Physicochemical Properties of Flaxseed Mucilage," *Journal of Advance Agricultural Research* 14 (2009): 605–621.

28. R. W. Fedeniuk and C. G. Biliaderis, "Composition and Physicochemical Properties of Linseed (Linum usitatissimum L.) Mucilage," *Journal of Agricultural and Food Chemistry* 42 (1994): 240–247, https://doi.org/10.1021/jf00038a003.

29. D. G. Easterby and J. K. N. Jones, "Composition of Linseed Mucilage," *Nature* 165 (1950): 614–614, https://doi.org/10.1038/165614a0.

30. M. S. Rocha, L. C. Rocha, M. B. S. Feijó, P. L. L. S. Marotta, and S. C. Mourao, "Effect of pH on the Flaxseed (Linum usitatissimum L. seed) Mucilage Extraction Process," *Acta Scientiarum Technology* 43 (2021): 50457, https://doi.org/10.4025/actascitechnol.v43i1.50457.

31. Y. Wang, Z. Wang, W. K. Pang, et al., "Solvent Control of Water O—H Bonds for Highly Reversible Zinc Ion Batteries," *Nature Communications* 14 (2023): 2720, https://doi.org/10.1038/s41467-023-38384-x.

32. W. Yang, Y. Yang, H. Yang, and H. Zhou, "Regulating Water Activity for Rechargeable Zinc-ion Batteries: Progress and Perspective," *ACS Energy Letters* 7 (2022): 2515–2530, https://doi.org/10.1021/acsenergylett.2c01152.

33. G. Subramani and R. Manian, "Production of Ferulic Acid From Dried Bamboo Shoots for the Biotransformation Into Vanillin Using a Novel Microbe Enterobacter aerogenes," *Biomass Conversion and Biorefinery* 13 (2023): 15211–15225, https://doi.org/10.1007/s13399-023-04891-6.

34. J. C. de Andrade Neto, G. J. Pereira, and A. A. Morandim-Giannetti, "Chitosan and Corn Stover Derivative Bioadsorbent: Characterization and Application in Hexavalent Chromium Adsorption Processes," *Cellulose* 27 (2020): 6317–6331, https://doi.org/10.1007/s10570-020-03240-4.

35. L. Zhao, Y. Li, M. Yu, Y. Peng, and F. Ran, "Electrolyte-Wettability Issues and Challenges of Electrode Materials in Electrochemical Energy Storage, Energy Conversion, and Beyond," *Advanced Science* 10 (2023): 2300283.

36. F. Zhao, Z. Jing, X. Guo, et al., "Trace Amounts of Fluorinated Surfactant Additives Enable High Performance Zinc-ion Batteries," *Energy Storage Materials* 53 (2022): 638–645, https://doi.org/10.1016/j.ensm.2022.10.001.

37. A. Wu, S. Zhang, Q. Li, et al., "Multifunctional Crown Ether Additive Regulates Desolvation Process to Achieve Highly Reversible Zinc-Metal Batteries," *Advanced Energy Materials* 15 (2025): 2404450.

38. P. Boguta and Z. Sokołowska, "Zinc Binding to Fulvic acids: Assessing the Impact of pH, Metal Concentrations and Chemical Properties of Fulvic Acids on the Mechanism and Stability of Formed Soluble Complexes," *Molecules* 25 (2020): 1297.

39. Z. Khan, D. Kumar, and X. Crispin, "Does Water-in-Salt Electrolyte Subdue Issues of Zn Batteries?," *Advanced Materials* 35 (2023): 2300369, https://doi.org/10.1002/adma.202300369.

40. Y. Avni, R. M. Adar, D. Andelman, and H. Orland, "Conductivity of Concentrated Electrolytes," *Physical Review Letters* 128 (2022): 098002, https://doi.org/10.1103/PhysRevLett.128.098002.

41. M. Bes˘ter Rogac˘, V. Babic˘, T. M. Perger, R. Neueder, and J. Barthel, "Conductometric Study of Ion Association of Divalent Symmetric Electrolytes: I. $CoSO_4$, $NiSO_4$, $CuSO_4$ and $ZnSO_4$ in Water," *Journal of Molecular Liquids* 118 (2005): 111–118, https://doi.org/10.1016/j.molliq.2004.07.023.

42. B. Ren, X. Zhang, H. Wei, et al., "Suppressing Zinc Metal Corrosion by an Effective and Durable Corrosion Inhibitor for Stable Aqueous Zinc Batteries," *Advanced Functional Materials* 35 (2025): 2418594, https://doi.org/10.1002/adfm.202418594.

43. B. Sui, W. Song, L. Sha, et al., "Citric Acid Etched Zinc Anode Surface to Improve the Stability of Aqueous Zinc-ion Battery," *Solid State Ionics* 405 (2024): 116437, https://doi.org/10.1016/j.ssi.2023.116437.

44. J. Shi, T. Sun, J. Bao, et al., ""Water-in-Deep Eutectic Solvent" Electrolytes for High-Performance Aqueous Zn-Ion Batteries," *Advanced Functional Materials* 31 (2021): 2102035, https://doi.org/10.1002/adfm.202102035.

45. C. Meng, W. He, L. Jiang, et al., "Ultra-Stable Aqueous Zinc Batteries Enabled by β-Cyclodextrin: Preferred Zinc Deposition and Suppressed Parasitic Reactions," *Advanced Functional Materials* 32 (2022): 2207732, https://doi.org/10.1002/adfm.202207732.

46. Y. Wang, L. Mo, X. Zhang, et al., "Regulating Water Activity for All-Climate Aqueous Zinc-Ion Batteries," *Advanced Energy Materials* 14 (2024): 2402041.

47. Z. Wang, J. Diao, J. N. Burrow, et al., "Urea-Modified Ternary Aqueous Electrolyte With Tuned Intermolecular Interactions and Confined Water Activity for High-Stability and High-Voltage Zinc-Ion Batteries," *Advanced Functional Materials* 33 (2023): 2304791, https://doi.org/10.1002/adfm.202304791.

48. Q. Meng, Q. Bai, R. Zhao, et al., "Attenuating Water Activity Through Impeded Proton Transfer Resulting from Hydrogen Bond Enhancement Effect for Fast and Ultra-Stable Zn Metal Anode," *Advanced Energy Materials* 13 (2023): 2302828.

49. S. Liu, L. Kang, J. M. Kim, Y. T. Chun, J. Zhang, and S. C. Jun, "Recent Advances in Vanadium-Based Aqueous Rechargeable Zinc-Ion Batteries," *Advanced Energy Materials* 10 (2020): 2000477, https://doi.org/10.1002/aenm.202000477.

Supporting Information

Additional supporting information can be found online in the Supporting Information section.

Supporting file: adsu70364-sup-0001-SuppMat.docx.